Optimal ultraviolet wavelength for *in vivo* photoacoustic imaging of cell nuclei

Da-Kang Yao
Ruimin Chen
Konstantin Maslov
Qifa Zhou
Lihong V. Wang

SPIE

Optimal ultraviolet wavelength for *in vivo* photoacoustic imaging of cell nuclei

Da-Kang Yao,[a] **Ruimin Chen,**[b] **Konstantin Maslov,**[a] **Qifa Zhou,**[b] **and Lihong V. Wang**[a]
[a]Washington University in St. Louis, Department of Biomedical Engineering, St. Louis, Missouri 63130
[b]University of Southern California, Department of Biomedical Engineering, Los Angeles, California 90089

Abstract. In order to image noninvasively cell nuclei *in vivo* without staining, we have developed ultraviolet photoacoustic microscopy (UV-PAM), in which ultraviolet light excites nucleic acids in cell nuclei to produce photoacoustic waves. Equipped with a tunable laser system, the UV-PAM was applied to *in vivo* imaging of cell nuclei in small animals. We found that 250 nm was the optimal wavelength for *in vivo* photoacoustic imaging of cell nuclei. The optimal wavelength enables UV-PAM to image cell nuclei using as little as 2 nJ laser pulse energy. Besides the optimal wavelength, application of a wavelength between 245 and 275 nm can produce *in vivo* images of cell nuclei with specific, positive, and high optical contrast. © *2012 Society of Photo-Optical Instrumentation Engineers (SPIE).* [DOI: 10.1117/1.JBO.17.5.056004]

1 Introduction

In order to determine cancer malignancy, pathologists first must find the malignant cells in cancer lesions.[1] The nuclei in cancer cells have typical morphological features, such as irregular shapes and large sizes,[2–4] which allow pathologists to identify cancer cells through microscopic examination of lesions. Optical microscopy of cell nuclei is the primary histological method, widely used for cancer diagnosis and malignancy grading.[5] Recently, several modern optical microscopy technologies have been explored for *in vivo* imaging of cell nuclei, including reflectance confocal microscopy,[6–9] multiphoton microscopy,[10–12] third-harmonic generation microscopy,[13,14] and ultraviolet photoacoustic microscopy (UV-PAM).[15] Without staining cell nuclei, reflectance confocal microscopy relies on the difference in refractive indices between cell nuclei and other tissue microstructures for image contrast.[6,8] However, the refractive index of cell nuclei is unspecific in tissues, which prevents reflectance confocal microscopy from providing specific image contrast for nuclei.[6] Multiphoton microscopy produces *in vivo* images of cell nuclei by detecting autofluorescence of reduced nicotinamide adenine dinucleotide (NADH).[11] Because NADH, a coenzyme in mitochondria, is located in cytoplasm around cell nuclei, multiphoton images show cell nuclei in negative contrast;[11,12,16] hence, multiphoton microscopy cannot image subnuclear structures such as nucleoli. Third harmonic light is generated by lipid bodies and collagen in tissue.[17,18] Third harmonic generation microscopy can employ backscattered third harmonic light to construct images of tissue structure, even though the image contrast is relatively low for cell nuclei.[13,14] In contrast, UV-PAM produces *in vivo* images of unstained cell nuclei with specific, positive, and high-image contrast.

UV-PAM is a new technique capable of specifically imaging of cell nuclei.[15] In UV-PAM, a pulsed laser beam of ultraviolet light (UV) is focused into biological tissue. DNA and RNA, two major components of cell nuclei, strongly absorb UV light at wavelengths around 260 nm.[19,20] The absorbed light is converted into heat in the nuclei. Thermoelastic expansion generates ultrasonic waves, which are detected as photoacoustic signals by a focused ultrasonic transducer. The photoacoustic signals are then processed to produce an image with positive contrast for the cell nuclei. Although DNA and RNA in cell nuclei strongly absorb UV light at 260 nm, proteins in the cytoplasm can absorb UV light as well.[21] As a result, the UV absorption of proteins produces a background in the image. Therefore, the contrast of cell nuclei in a photoacoustic image depends on the difference in UV absorption between cell nuclei and the cytoplasm, which varies with the optical wavelength. Using light with a wavelength of 266 nm, we have shown that the photoacoustic imaging technique can generate high contrast *in vivo* images of nuclei.[15] Other than the 266-nm wavelength, various UV wavelengths are available within the absorption spectra of DNA and RNA, but it is not known whether these wavelengths can yield high contrast *in vivo* images of nuclei. In particular, the optimal wavelength, which can yield the best image contrast, is not known for *in vivo* photoacoustic imaging of cell nuclei. In order to find the optimal wavelength, we imaged cell nuclei in mouse ear skin *in vivo* at various wavelengths, using a UV-PAM system with a tunable laser.

2 Materials and Methods

2.1 Animal Preparation

Four female athymic nude mice were purchased from Harlan Laboratories (Indianapolis, IN). The mice were anesthetized with 1% isoflurane (Butler Animal Health Supply, Dublin, OH) delivered in pure oxygen (Airgas, St. Louis, MO) at a flow

Address all correspondence to: Lihong V. Wang, Washington University in St. Louis, Department of Biomedical Engineering, Optical Imaging Laboratory, One Brookings Drive, Campus Box 1097, St. Louis, Missouri 63130. Tel.: +3149356152; Fax: +3149357448; E-mail: lhwang@biomed.wustl.edu
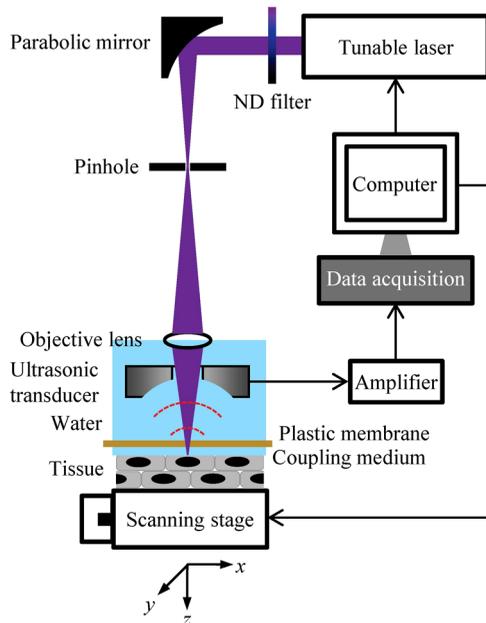
Fig. 1 Schematic of the ultraviolet photoacoustic microscopy system with a tunable laser system. ND: neutral density.

rate of 0.5 L/min. Before imaging, the mouse ear skin was gently washed three times using distilled water. After imaging, and the inhalational anesthesia was stopped, the mice recovered in 10 min. All experimental animal procedures were carried out in conformity with the laboratory animal protocol of the Animal Studies Committee of Washington University in St. Louis.

2.2 Ultraviolet Photoacoustic Microscopy

A detailed description of the original UV-PAM system was reported previously.[15] In order to investigate the optimal wavelength for *in vivo* photoacoustic imaging of cell nuclei, we equipped the UV-PAM system with an OPO laser system (NT242-SH, Altos Photonics, Bozeman, MT) that provides a wavelength tuning range from 210 to 2300 nm.[22] Figure 1 is a schematic of the improved UV-PAM system. A pulsed UV laser beam with a pulse width of 5 ns is emitted from the tunable laser system at a repetition rate of 1 kHz. After being attenuated by a neutral density filter (NDC-50C-4M, Thorlabs, Newton, NJ), the laser beam is focused by a 100-mm-focal-length off-axis parabolic mirror (50338AL, Newport, Irvine, CA), and then spatially filtered by a 25-μm-diameter pinhole (910PH-25, Newport). The beam is refocused into a water tank by a 0.1 NA objective lens (LA4280, Thorlabs), passes through a focused ring ultrasonic transducer (50 MHz central frequency, 7 mm focal length), and penetrates a 25-μm-thick polyethylene
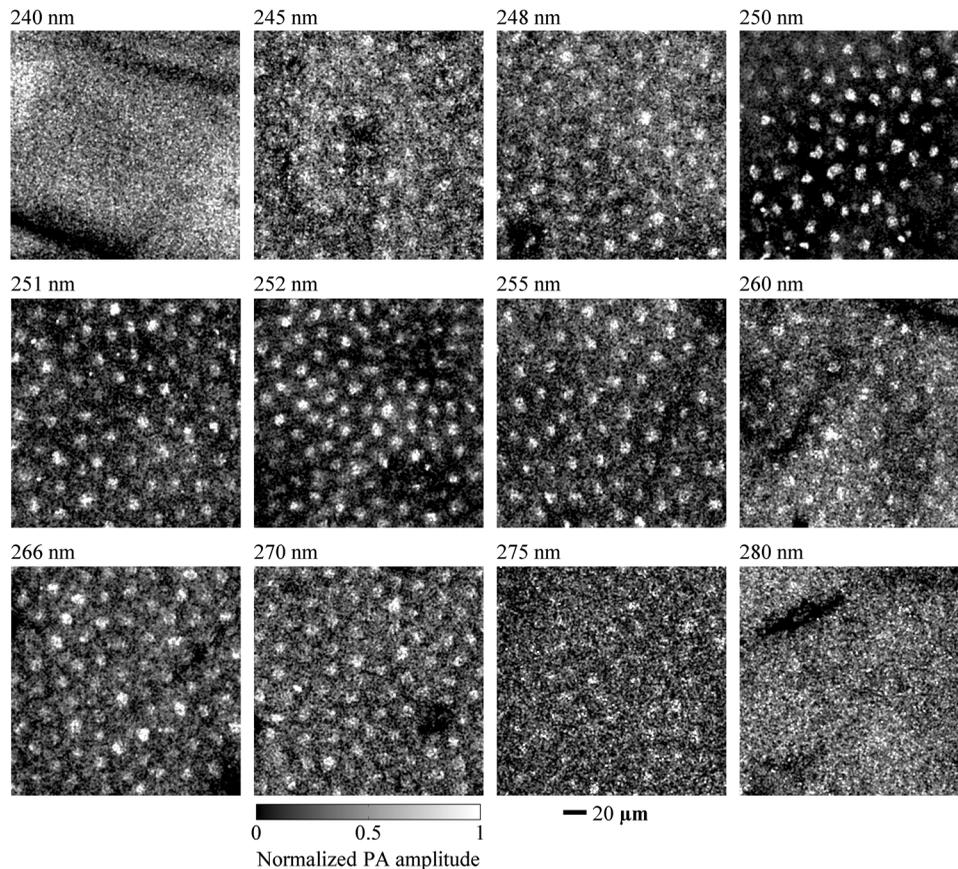
Fig. 2 *In vivo en face* photoacoustic images of the skin of mouse ears in the form of maximum amplitude projection (MAP). The images were acquired by using wavelengths of 240, 245, 248, 250, 251, 252, 255, 260, 266, 270, 275, and 280 nm, respectively. Cell nuclei in the mouse skin are shown in the images at 245, 248, 250, 251, 252, 255, 260, 266, 270, and 275 nm but are unidentifiable in the images at 240 and 280 nm. PA: photoacoustic.

membrane before focusing along the *z* axis to an object. The ultrasonic transducer is coaxially aligned with the objective lens to a common focus. The polyethylene membrane forms an optical window on the bottom of the water tank and maintains acoustic coupling. The laser pulse energy behind the membrane is measured by a digital power meter (PM100D, Thorlabs) with a silicon photodiode sensor (S120VC, Thorlabs). The water tank and the specimen are mounted on a translation stage (PT1, Thorlabs), which is vertically installed on a two-dimensional scanning stage (Micos USA, Irvine, CA) for manual focusing of the specimen. While the scanning stage performs raster scanning with a step size of 0.62 μm in the horizontal plane (*x*–*y* plane), photoacoustic signals are detected by the ultrasonic transducer, amplified by an amplifier (ZFL-500LN, Mini-Circuits, Branson, MO), and collected by a computer through a 12-bit, 200 MHz digitizer (NI PCI-5124, National Instruments, Austin, TX).

Tomographic images are formed from the amplitude envelopes of the time-resolved photoacoustic signals. Each laser pulse produces a time-resolved photoacoustic signal. Hilbert transformation of the signal produces its amplitude envelope along the *z*-axis. A collection of the envelopes along the *x*-axis produces a cross-sectional image in the *x*–*z* plane, a B-scan image.[23] Further scanning along the *y*-axis produces three-dimensional images. Projection of the maximal amplitude of each envelope to the scanning plane (*x*–*y* plane) produces a maximum amplitude projection (MAP) image.[24,25] By using 266 nm light, our UV-PAM system achieves 0.7-μm lateral resolution and 28-μm axial (*z*-axis) resolution.[15] It took 2.6 min to acquire an image of $200 \times 200 \ \mu m^2$.

2.3 Morphometric Analysis

In order to analyze epidermal images obtained by reflectance confocal microscopy, Gareau[26] constructed an error function to model the intensity profile of the nuclear image. He obtained the nuclear diameter of epidermal keratinocytes by fitting the error function to the image after normalization. Here, we adapted the error function to analyze non-normalized photoacoustic images of cell nuclei. For a nuclear image with positive contrast, the image intensity (*I*) profile is approximated by an error function (erf) as

$$I(x,y) = A\text{erf}\left[\frac{R - \sqrt{(x-x_0)^2 + (y-y_0)^2}}{C}\right] + B, \quad (1)$$

where x_0 and y_0 are coordinates of the center of the cell nucleus; *R* is the radius of the nucleus; *A* and *B* are the relative intensity and the background intensity of the image, respectively; and *C* is a constant. The six parameters, x_0, y_0, *R*, *A*, *B*, and *C*, are determined by nonlinear least-squares fitting.

3 Results

3.1 Wavelength Range

Using various wavelengths, we imaged cell nuclei *in vivo* in the ear skin of mice. An anesthetized mouse was held by a custom-made stereotaxic imaging stage. After the imaging stage was mounted on the translational stage, a mouse ear was flat placed on a plastic plate immobilized on the imaging stage, and then the image window was lowered to be in contact with a film of distilled water on the mouse ear. During the preview scanning, we

adjusted the translational stage upward until a clear B-scan image was observed. Then, we scanned the ear skin with laser pulse energy of 20 nJ at wavelengths ranging from 220 to 310 nm. We repeated the experiments twice at wavelengths of 245, 248, 250, 251, 252, 255, 260, 266, 270, and 275 nm. Both experiments yielded identifiable images of cell nuclei. Typical images are shown in Fig. 2. However, for wavelengths of 220, 230, 240, 280, 290, 300, and 310 nm, we repeated imaging experiments two to five times, but did not obtain any identifiable image of cell nuclei. Two typical images of mouse ear skin acquired at wavelengths of 240 and 280 nm are shown in Fig. 2. All of these images show that wavelengths ranging from 245 to 275 nm are most applicable to *in vivo* photoacoustic imaging of unstained cell nuclei.
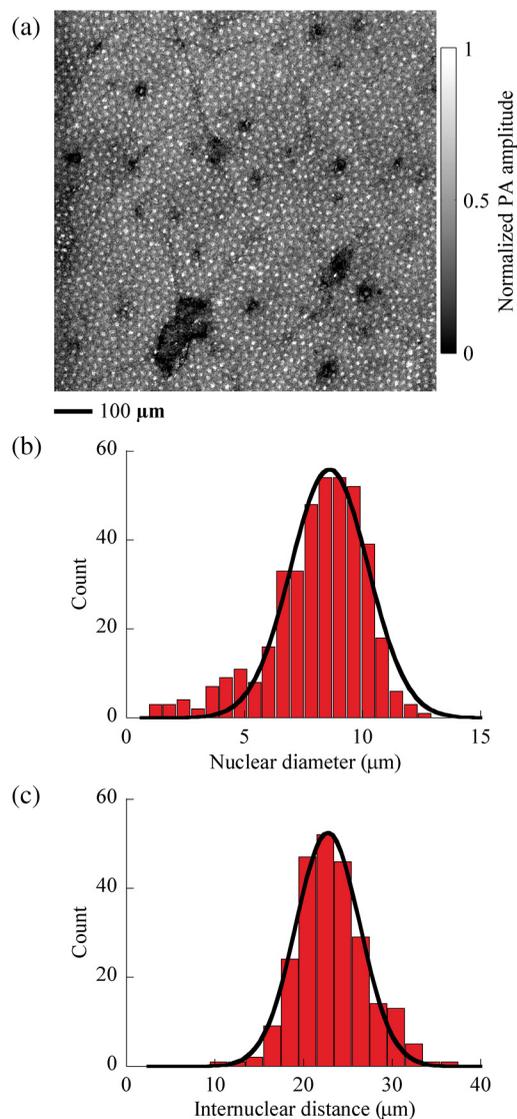
Fig. 3 *In vivo en face* distribution of cell nuclei in the skin of mouse ears. (a) *In vivo* MAP photoacoustic image of cell nuclei distributed in 1 mm^2 mouse skin, acquired at a wavelength of 250 nm. PA: photoacoustic. (b) Histogram of the nuclear diameter ($n = 404$). Bin width is 0.6 μm. The solid curve is a Gaussian fit with a mean of 8.6 μm and a standard deviation (SD) of 1.6 μm (coefficient of determination $R^2 = 0.96$). (c) Histogram of the internuclear distance ($n = 245$). Bin width is 2 μm. The solid curve is a Gaussian fit with a mean of 22.7 μm and a SD of 3.6 μm ($R^2 = 0.98$).
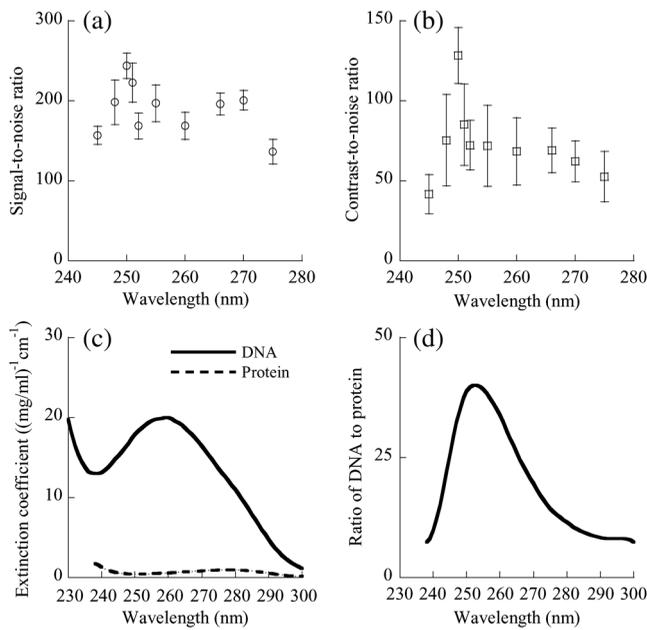
Fig. 4 Signal and contrast of *in vivo* photoacoustic images of cell nuclei versus the optical wavelength. (a) Plot of SNR (mean ± SD) of nuclear images versus wavelength. The SNR was collected from 25 cell nuclei in MAP photoacoustic images for each wavelength. (b) Plot of CNR (mean ± SD) of nuclear images versus wavelength. The mean was calculated from 25 nuclei. (c) Typical absorption spectra of DNA and protein. The DNA is thymus DNA, and the protein is glutamate dehydrogenase. The absorption spectrum of DNA is adapted from Kunitz (1950) and Sambrook et al. (2001), and that of protein from Olson et al. (1952) and Gill et al. (1989). (d) The ratio of DNA to protein, defined as the ratio of the absorption coefficient of thymus DNA to that of glutamate dehydrogenase.

3.2 Nuclear Diameter and Internuclear Distance

We examined the distributions of the diameters of cell nuclei and the distance between the centers of neighboring cell nuclei, or the internuclear distance, in the mouse ear skin. Figure 3(a) is an *in vivo* MAP image acquired at 250 nm with laser pulse energy of 20 nJ. As shown, the nuclei of keratinocytes are evenly distributed in the skin. To measure the diameter of a single cell nucleus, we selected a square window with 31 × 31 pixels to enclose the nucleus image, with the window center close to the nucleus center. Iterative fitting within the square window to Eq. (1) produced both the radius and the center coordinates of the cell nucleus. After fitting 404 cell nuclei in Fig. 3(a), we obtained a histogram of the nuclear diameter of keratinocytes in the mouse skin, shown in Fig. 3(b). We fitted the histogram using a Gaussian function, and found that the nuclear diameter was 8.6 ± 1.6 μm (mean ± SD) for keratinocytes in the mouse skin. Among the aforementioned 404 cell nuclei, 245 pairs of neighboring cell nuclei were chosen to calculate the internuclear distance. Figure 3(c) is a histogram of the internuclear distance of keratinocytes in the mouse skin. After fitting a Gaussian function to the histogram, we found that the internuclear distance was 22.7 ± 3.6 μm (mean ± SD).

3.3 Optimal Wavelength

We examined the signal-to-noise ratio (SNR) and the contrast-to-noise ratio (CNR) of the photoacoustic images of cell nuclei as functions of the optical wavelength. All the images were acquired with laser pulse energy of 20 nJ. The mean intensity of the image of a single cell nucleus was obtained by averaging the amplitude within a square window of 10 × 10 pixels in the
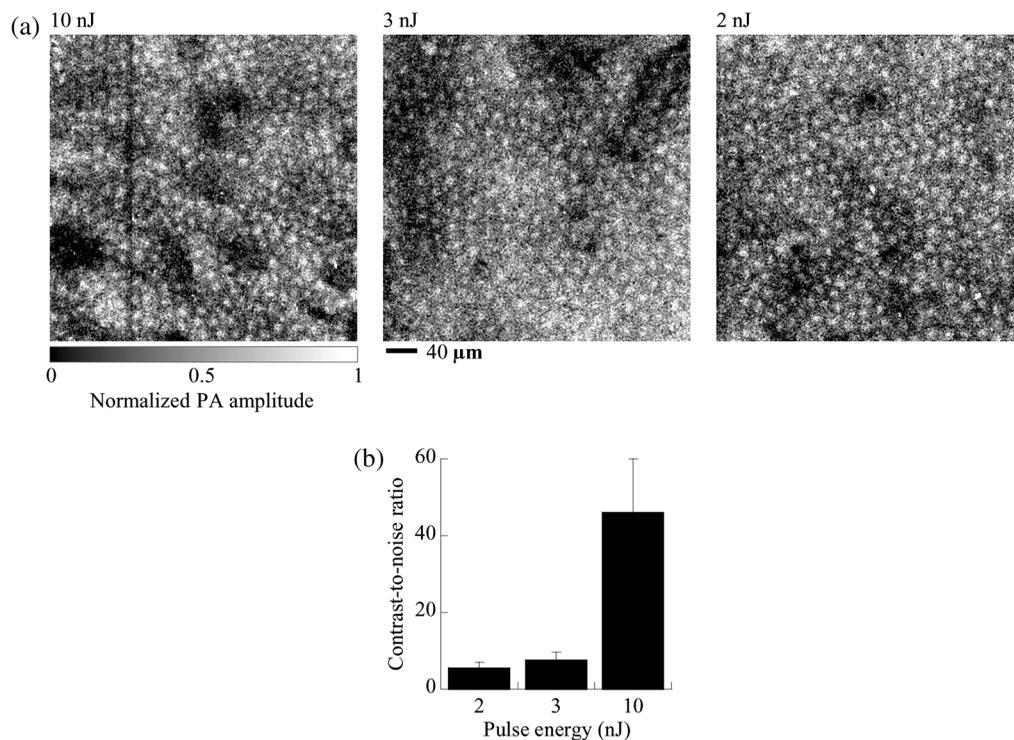
Fig. 5 *In vivo* photoacoustic imaging of cell nuclei in the skin of mouse ears with varied laser pulse energy at a wavelength of 250 nm. (a) *In vivo* MAP photoacoustic images of cell nuclei at pulse energies of 10, 3, and 2 nJ. PA: photoacoustic. (b) CNR (mean ± SD) of the nuclear images. The CNR was collected from 25 cell nuclei in MAP photoacoustic images for each pulse energy.

image of the cell nucleus. The diameter of cell nuclei is ~8.6 μm, approximately 14 pixels. Hence, if the cell nucleus image is assumed as a solid circle, a window of 10×10 pixels is an inscribed square in the circle. The distance between the centers of neighboring nuclei is ~22.7 μm, approximately 36 pixels. Thus, a square window of 30×30 pixels concentric with a single nuclear image does not cover neighboring nuclei, and a square window of 20×20 pixels concentric with the former window totally covers the single nuclear image. Inside the larger window but outside the smaller one, we calculated the mean intensity of the background image surrounding the nuclear image. In order to measure image noise, we scanned the mouse ear using zero laser output in each experiment. A dummy photoacoustic image was formed with zero laser output and was used to compute the standard deviation of image intensity. For each wavelength between 245 and 275 nm, we calculated the SNR and CNR of the MAP images of 25 cell nuclei. After averaging, we obtained the dependence of image SNR on wavelength, as shown in Fig. 4(a), and the dependence of CNR on wavelength, as shown in Fig. 4(b). Both SNR and CNR significantly change with the wavelength, and each reaches its maximum at a wavelength of 250 nm. Although application of a 266 nm wavelength generated *in vivo* photoacoustic images of cell nuclei with high image contrast, the CNR at 250 nm was 1.9 times greater than that at 266 nm, and the SNR at 250 nm was 1.2 times higher than that at 266 nm. Therefore, 250 nm was deemed the optimal wavelength for *in vivo* photoacoustic imaging of unstained cell nuclei.

3.4 *Low Energy Imaging*

The optimal wavelength allows UV-PAM to use low laser energy for *in vivo* imaging of cell nuclei. We repeated the *in vivo* imaging experiment using 250 nm light but low laser pulse energy. Instead of 20 nJ, the laser pulse energy was set to 10, 3, and 2 nJ, yielding three *in vivo* MAP images of cell nuclei in the mouse ear skin shown in Fig. 5(a). The photoacoustic images clearly show the regular distribution of cell nuclei in the skin and the nuclear size of individual keratinocytes, even though the laser pulse energy is as low as 2 nJ. Figure 5(b) shows the average CNR of the nuclear images at pulse energies of 2, 3, and 10 nJ. The average CNR is 46.1 at 10 nJ, 7.7 at 3 nJ, and 5.5 at 2 nJ. Therefore, the pulse energy limit is less than 2 nJ for *in vivo* imaging of cell nuclei.

4 Discussion and Conclusions

Exploring the absorption spectra of nucleic acids and cytoplasmic proteins, we found the optimal wavelength for *in vivo* photoacoustic imaging of cell nuclei. Although *in vivo* images of cell nuclei were acquired at wavelengths ranging from 245 to 275 nm, the 250 nm wavelength enabled UV-PAM to produce the highest contrast *in vivo* image. In UV-PAM, the image contrast relies on the difference in light absorption between nucleic acids and cytoplasmic proteins, such as thymus DNA and glutamate dehydrogenase. Thymus DNA is a typical DNA, and glutamate dehydrogenase is one of cytoplasmic proteins; their absorption spectra are shown in Fig. 4(c).[27–30] The ratio of the absorption coefficient of DNA to that of cytoplasmic protein is plotted versus wavelength in Fig. 4(d). This ratio reflects the absorption contrast between DNA and cytoplasmic protein. It is shown that the absorption spectrum of DNA has its peak at 260 nm, and the absorption peak of cytoplasmic protein is at 280 nm. Nevertheless, the ratio of DNA absorption

to cytoplasmic protein absorption reaches its peak at 252 nm, close to the experimentally identified 250 nm, suggesting that the optimal wavelength results from the maximal absorption ratio between nucleic acids and cytoplasmic proteins. Furthermore, Fig. 4 shows that the CNR distribution of the nuclear image is quite consistent with the distribution of the DNA-to-protein ratio. Although the image CNR of cell nuclei was collected through imaging the skin of mouse ears, the ratio of DNA to protein is independent of tissue types, suggesting that the optimal wavelength is useful to photoacoustic imaging of cell nuclei in various other tissues.

Tissue photodamage caused by UV light should be controlled for *in vivo* photoacoustic imaging of cell nuclei. Using a laser pulse energy of 20 nJ, we scanned a 1×1 mm² area of the mouse ear skin. After continuously scanning the same area three times, we observed skin redness. One day after the scanning, we observed inflammation in the skin, indicating severe photodamage. However, no visible damage was observed after scanning the mouse skin only once. For example, after one raster scan, we found no distinguishable color change in the skin. Continuing observation for a week did not reveal any inflammation in the mouse skin, suggesting negligible photodamage. Therefore, when we imaged the mouse ear skin using 20 nJ pulse energy, we did not repeatedly scan a similar skin area in one experiment. However, repeated scans of the same skin area may be practicable with lower pulse energy, such as 2 nJ. We imaged an area of the mouse ear skin twice using 2 nJ pulse energy at a wavelength of 250 nm, and did not see any photodamage. Another possible approach to minimize photodamage is to use a larger beam area and a greater scanning step size. For clinical applications, skin exposure to a UV beam is limited by the safety standard defined by the American National Standards Institute (ANSI), which sets the maximum permissible exposure (MPE) at 3 mJ/cm² for wavelengths between 180 and 302 nm.[31] It is understood that the safety standard is set far below the damage threshold.[32] In our experiments, the imaged cell nuclei were about 30 μm deep below the skin surface. If it is assumed that the laser beam focused on the nuclei follows a Gaussian beam profile, the cross-sectional area of the 250-nm-wavelength laser beam on the skin surface is 30 μm². The radiant exposure to the mouse skin is estimated to be 66 mJ/cm² for 20 nJ pulse energy and 6.6 mJ/cm² for 2 nJ pulse energy, both of which are higher than the MPE. If the cell nuclei to be imaged are 50 μm deep, the beam cross-sectional area on the skin surface is 81 μm². We estimate that the skin radiant exposure is 25 mJ/cm² for 20 nJ pulse energy, which is greater than the MPE, but 2.5 mJ/cm² for 2 nJ pulse energy, which is less than the MPE.

Distilled water was chosen for ultrasound coupling instead of ultrasound gel. We found that ultrasound gel strongly absorbed UV light at wavelengths between 220 and 310 nm. When ultrasound gel was used as a coupling medium, SNR measurements lacked repeatability, likely from different thicknesses of the coupling medium, which caused different light attenuation. Thus, although widely used in photoacoustic imaging,[33–35] ultrasound gel is not an ideal coupling medium for UV-PAM. Repeatable measurements were obtained using distilled water as an ultrasound coupling medium. We could continuously image the mouse skin for four hours until the water under the image window began evaporation.

This is the first time that the nuclear diameter and internuclear distance of epidermal cells in the skin of mouse ears have

been measured *in vivo*. We found that the *in vivo* nuclear diameter of the epidermal cells was 8.6 ± 1.6 μm, and the *in vivo* internuclear distance of the epidermal cells was 22.7 ± 3.6 μm. Using reflectance confocal microscopy, Gareau[26] finds that the nuclear diameter is 8.6 ± 2.8 μm for the keratinocytes in a melanocytic nevus, similar to the nuclear diameter of mouse epidermal cells. Using third harmonic microscopy, Chen et al.[14] find that the average internuclear distance is 19.9 μm for granular keratinocytes in the skin of human forearms, approximate to the internuclear distance of mouse epidermal cells. The approximation reflects comparable *en face* morphologies of the epidermis between human beings and mice. The *in vivo* nuclear diameter and internuclear distance of mouse epidermal cells are useful in biological studies. For example, using transgenic mice, biologists find that change in the nuclear diameter is related to tumorigenic activities in epidermis.[36,37]

A nonlinear photoacoustic behavior is observed in Fig. 5(b), where the CNR is not proportional to laser pulse energy. In this study, the waist diameter of the focused laser beam measured 1.5 μm. When the focused laser pulse heats a cell nucleus, each pulse produces a small thermal source. Thermal diffusion from the small source generates photoacoustic waves in tissue.[38] The thermal expansion coefficient of tissue changes with temperature.[39] In photoacoustics, if the expansion coefficient linearly increases with temperature, the photoacoustic signal amplitude quadratically increases with light fluence.[38] Therefore, the nonlinear thermal expansion of skin tissue causes the nonlinear behavior between the photoacoustic signal amplitude and the laser pulse energy.

In conclusion, UV-PAM is able to image cell nuclei *in vivo* with specific, positive, and high contrast. We found that 250 nm was the optimal wavelength for the highest optical contrast. The optimal wavelength enabled UV-PAM to image cell nuclei *in vivo* using only 2 nJ of laser pulse energy. In addition, any wavelength between 245 and 275 nm can also be used to produce *in vivo* images of cell nuclei.

Acknowledgments

References

1. J. L. Connolly et al., "Principles of cancer pathology," in *Holland-Frei Cancer Medicine* **8**, W. K. Hong et al., Eds., People's Medical Publishing House-USA, Shelton, CT (2010).
2. L. D. True and C. D. Jordan, "The cancer nuclear microenvironment: Interface between light microscopic cytology and molecular phenotype," *J. Cell. Biochem.* **104**(6), 1994–2003 (2008).
3. D. Zink, A. H. Fischer, and J. A. Nickerson, "Nuclear structure in cancer cells," *Nat. Rev. Cancer* **4**(9), 677–687 (2004).
4. J. A. Nickerson, "Nuclear dreams: The malignant alteration of nuclear architecture," *J. Cell. Biochem.* **70**(2), 172–180 (1998).
5. S. C. Lester, *Manual of Surgical Pathology*, Saunders/Elsevier, Philadelphia (2010).
6. K. S. Nehal, D. Gareau, and M. Rajadhyaksha, "Skin imaging with reflectance confocal microscopy," *Semin. Cutaneous Med. Surg.* **27**(1), 37–43 (2008).
7. P. J. Dwyer et al., "Confocal reflectance theta line scanning microscope for imaging human skin in vivo," *Opt. Lett.* **31**(7), 942–944 (2006).
8. S. Gonzalez and Z. Tannous, "Real-time, in vivo confocal reflectance microscopy of basal cell carcinoma," *J. Am. Acad. Dermatol.* **47**(6), 869–874 (2002).
9. W. M. White et al., "Noninvasive imaging of human oral mucosa in vivo by confocal reflectance microscopy," *Laryngoscope* **109**(10), 1709–1717 (1999).
10. B. R. Masters, P. T. So, and E. Gratton, "Multiphoton excitation fluorescence microscopy and spectroscopy of in vivo human skin," *Biophys. J.* **72**(6), 2405–2412 (1997).
11. B. G. Wang, K. Konig, and K. J. Halbhuber, "Two-photon microscopy of deep intravital tissues and its merits in clinical research," *J. Microsc.* **238**(1), 1–20 (2010).
12. L. Chunqiang et al., "Multiphoton microscopy of live tissues with ultraviolet autofluorescence," *IEEE J. Sel. Top. Quantum Electron.* **16**(3), 516–523 (2010).
13. M. R. Tsai et al., "In vivo optical virtual biopsy of human oral mucosa with harmonic generation microscopy," *Biomed. Opt. Express* **2**(8), 2317–2328 (2011).
14. S. Y. Chen, H. Y. Wu, and C. K. Sun, "In vivo harmonic generation biopsy of human skin," *J. Biomed. Opt.* **14**(6), 060505 (2009).
15. D. K. Yao et al., "In vivo label-free photoacoustic microscopy of cell nuclei by excitation of DNA and RNA," *Opt. Lett.* **35**(24), 4139–4141 (2010).
16. S. J. Lin, S. H. Jee, and C. Y. Dong, "Multiphoton microscopy: a new paradigm in dermatological imaging," *Eur. J. Dermatol.* **17**(5), 361–366 (2007)..
17. D. Debarre et al., "Imaging lipid bodies in cells and tissues using third-harmonic generation microscopy," *Nat. Meth.* **3**(1), 47–53 (2006).
18. P. Friedl et al., "Biological second and third harmonic generation microscopy," in *Current Protocols in Cell Biology*, John Wiley & Sons, Inc. (2007).
19. A. V. Tataurov, Y. You, and R. Owczarzy, "Predicting ultraviolet spectrum of single stranded and double stranded deoxyribonucleic acids," *Biophys. Chem.* **133**(1–3), 66–70 (2008).
20. A. Fleck and D. Begg, "The estimation of ribonucleic acid using ultraviolet absorption measurements," *Biochim. Biophys. Acta, Nucleic Acids Protein Synth.* **108**(3), 333–339 (1965).
21. A. R. Goldfarb, L. J. Saidel, and E. Mosovich, "The ultraviolet absorption spectra of proteins," *J. Biol. Chem.* **193**(1), 397–404 (1951).
22. N. Savage, "Optical parametric oscillators," *Nat. Photonics* **4**(2), 124–125 (2010).
23. H. F. Zhang, K. Maslov, and L. V. Wang, "In vivo imaging of subcutaneous structures using functional photoacoustic microscopy," *Nat. Protoc.* **2**(4), 797–804 (2007).
24. H. F. Zhang et al., "Functional photoacoustic microscopy for high-resolution and noninvasive in vivo imaging," *Nat. Biotech.* **24**(7), 848–851 (2006).
25. J.-M. Yang et al., "Photoacoustic endoscopy," *Opt. Lett.* **34**(10), 1591–1593 (2009).
26. D. Gareau, "Automated identification of epidermal keratinocytes in reflectance confocal microscopy," *J. Biomed. Opt.* **16**(3), 030502 (2011).
27. M. Kunitz, "Crystalline desoxyribonuclease; isolation and general properties; spectrophotometric method for the measurement of desoxyribonuclease activity," *J. Gen. Physiol.* **33**(4), 349–362 (1950).
28. J. Sambrook and D. W. Russell, *Molecular Cloning: A Laboratory Manual*, Cold Spring Harbor Laboratory Press, Cold Spring Harbor, NY (2001).
29. S. C. Gill and P. H. von Hippel, "Calculation of protein extinction coefficients from amino acid sequence data," *Anal. Biochem.* **182**(2), 319–326 (1989).
30. J. A. Olson and C. B. Anfinsen, "The crystallization and characterization of L-glutamic acid dehydrogenase," *J. Biol. Chem.* **197**(1), 67–79 (1952).
31. American National Standards Institute, *American National Standard for Safe Use of Lasers : ANSI Z136.1-2007*, Laser Institute of America, Orlando (2007).
32. V. P. Zharov et al., "Photoacoustic flow cytometry: principle and application for real-time detection of circulating single nanoparticles, pathogens, and contrast dyes in vivo," *J. Biomed. Opt.* **12**(5), 051503 (2007).
33. S. Hu et al., "Label-free photoacoustic ophthalmic angiography," *Opt. Lett.* **35**(1), 1–3 (2010).

34. S. Hu et al., "Functional transcranial brain imaging by optical-resolution photoacoustic microscopy," *J. Biomed. Opt.* **14**(4), 040503 (2009).

35. X. Yang et al., "Photoacoustic tomography of small animal brain with a curved array transducer," *J. Biomed. Opt.* **14**(5), 054007 (2009).

36. P. L. Miliani de Marval et al., "Transgenic expression of cyclin-dependent kinase 4 results in epidermal hyperplasia, hypertrophy, and severe dermal fibrosis," *Am. J. Pathol.* **159**(1), 369–379 (2001).

37. P. L. Miliani de Marval et al., "Lack of cyclin-dependent kinase 4 inhibits c-myc tumorigenic activities in epithelial tissues," *Mol. Cell. Biol.* **24**(17), 7538–7547 (2004).

38. I. G. Calasso, W. Craig, and G. J. Diebold, "Photoacoustic point source," *Phys. Rev. Lett.* **86**(16), 3550–3553 (2001).

39. F. A. Duck, *Physical Properties of Tissue: A Comprehensive Reference Book*, Academic Press, London; San Diego (1990).